10-25-2017

Plasma Transport Driven by the Three-Dimensional Kelvin-Helmholtz Instability

Xuanye Ma
Embry-Riddle Aeronautical University, max@erau.edu

Peter Delamere
University of Alaska, Fairbanks

Antonius Otto
University of Alaska, Fairbanks

Brandon Burkholder
University of Alaska, Fairbanks

Scholarly Commons Citation

Ma, X., Delamere, P., Otto, A., & Burkholder, B. (2017). Plasma Transport Driven by the Three-Dimensional Kelvin-Helmholtz Instability. *Journal of Geophysical Research: Space Physics, 122*(10). https://doi.org/10.1002/2017JA024394

AGU PUBLICATIONS

JGR

Journal of Geophysical Research: Space Physics

RESEARCH ARTICLE

10.1002/2017JA024394

Plasma Transport Driven by the Three-Dimensional Kelvin-Helmholtz Instability

Xuanye Ma[1,2], **Peter Delamere**[1], **Antonius Otto**[1], **and Brandon Burkholder**[1]

[1]Geophysical Institute, University of Alaska Fairbanks, Fairbanks, AK, USA, [2]Now at Department of Physical Sciences, Embry-Riddle Aeronautical University, Daytona Beach, FL, USA

Key Points:
- Plasma transport by double reconnection driven by 3-D KH waves is more efficient than 2-D KH wave
- The total open flux is mostly determined by the boundary conditions, which strongly influence the plasma transport rate
- The theory of general magnetic reconnection does not apply to double reconnection

Correspondence to:
X. Ma,
max@erau.edu

Citation:
Ma, X., Delamere, P., Otto, A., & Burkholder, B. (2017), Plasma transport driven by the three-dimensional Kelvin-Helmholtz instability. *Journal of Geophysical Research: Atmospheres*, *122*, 10,382–10,395. https://doi.org/10.1002/2017JA024394

Received 23 MAY 2017
Accepted 23 AUG 2017
Accepted article online 28 AUG 2017
Published online 25 OCT 2017

Abstract It has been well demonstrated that the nonlinear Kelvin-Helmholtz (KH) instability plays a critical role for the solar wind interaction with the Earth's magnetosphere. Although the two-dimensional KH instability has been fully explored during the past decades, more and more studies show the fundamental difference between the two- and three-dimensional KH instability. For northward interplanetary magnetic field (IMF) conditions, the nonlinear KH wave that is localized in the vicinity of the equatorial plane can dramatically bend the magnetic field line, generating strong antiparallel magnetic field components at high latitudes in both North and South Hemispheres, which satisfy the onset condition for magnetic reconnection. This high-latitude double reconnection process can exchange the portion of magnetosheath and magnetospheric flux tubes between those two reconnection sites. This study used a high-resolution 3-D magnetohydrodynamic simulation to demonstrate that nonlinear KH waves can generate a large amount of double-reconnected flux during the northward IMF condition, which can efficiently transport the plasma with a high diffusion coefficient of 1×10^{10} m^2 s^{-1} for typical magnetopause conditions at the Earth. The presence of the magnetic field component along the shear flow direction not only decreases the KH growth rate but also causes north-south asymmetry, which generates more open flux and reduces the efficiency of the plasma transport process.

1. Introduction

The Kelvin-Helmholtz (KH) instability driven by a large sheared flow (Chandrasekhar, 1961) is often considered as one of the major mechanisms of the "viscous-like" interaction (Axford, 1964) between the solar wind and the Earth's magnetosphere during northward interplanetary magnetic field (IMF) conditions (Johnson et al., 2014). Nonlinear KH waves are ubiquitously observed by different spacecrafts (Chen & Kivelson, 1993; Eriksson et al., 2016; Fairfield et al., 2000; Hasegawa et al., 2004, 2006; Li et al., 2016; Nakamura et al., 2013; Nykyri et al., 2006; Stawarz et al., 2016; Vernisse et al., 2016) at low latitudes under both northward and southward IMF conditions (Hwang et al., 2011; Kavosi & Raeder, 2015; Walsh et al., 2015; Yan et al., 2014), as well as at high latitudes for dawnward and duskward IMF conditions (Hwang et al., 2012; Ma, Otto, Delamere, et al., 2016), which are consistent with global magnetohydrodynamics (MHD) simulations (Guo et al., 2010; Hwang et al., 2011; Li et al., 2012; Merkin et al., 2013). Therefore, it is of importance to identify and quantify how efficiently the nonlinear KH instability transports magnetic flux, mass, flux tube entropy, and momentum.

Two-dimensional (2-D) simulations with different descriptions (i.e., MHD, Hall MHD, and two fluid simulations) demonstrated that nonlinear KH waves can dramatically twist magnetic field lines if the boundary conditions have small magnetic field components along the sheared flow direction. Such a process can generate large antiparallel magnetic components and consequently trigger magnetic reconnection, even if the initial boundary conditions have no magnetic shear. Thus, plasma can be transported from the solar wind into Earth's magnetosphere via the nonlinear KH instability (Otto & Fairfield, 2000; Nakamura & Fujimoto, 2005; Nakamura et al., 2006, 2008; Nykyri & Otto, 2001, 2004). For typical magnetopause conditions at the Earth, MHD, Hall MHD, and hybrid simulations quantified that the diffusion coefficients via the 2-D KH instability are on the order of 10^9 m^2 s^{-1} (Cowee et al., 2009, 2010; Nykyri & Otto, 2001, 2004). This value is close to the canonical diffusivity required to populate the low-latitude boundary layer (Sonnerup, 1980). Furthermore, at Saturn's magnetopause, the diffusion coefficient due to KH plasma mixing is expected to be more than 10^{10} m^2 s^{-1} (Delamere et al., 2011), which can play a significant role in driving magnetospheric dynamics.

The nonlinear dynamics of the KH instability in three-dimensional (3-D) configurations is fundamentally different compared with two dimensions (Otto, 2008). Both the KH instability and magnetic reconnection can

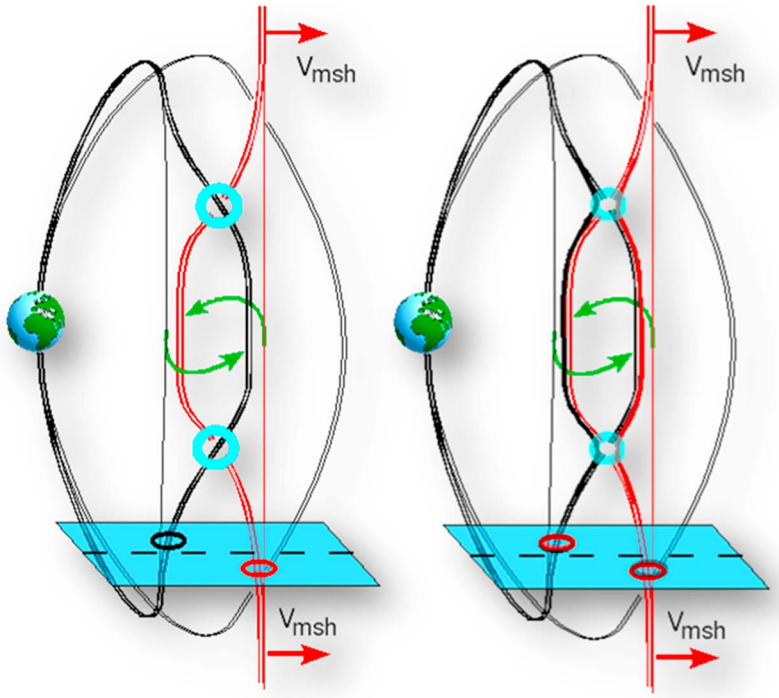

Figure 1. Sketch of 3-D KH instability. The black and red lines are represented for the closed magnetospheric field line and solar wind field line before (left) and after (right) high-latitude double reconnection operates, respectively. The blue circles highlight the high-latitude reconnection sites.

operate simultaneously under southward IMF conditions (Chen, 1997; Chen et al., 1997). A fast Petschek reconnection rate can be achieved during the nonlinear interaction between the KH instability and a magnetic reconnection event without including kinetic physics, but the total open flux is limited (Ma et al., 2014a, 2014b). Although a strong tangential magnetic field component around the magnetopause under Parker-Spiral IMF conditions tends to stabilize the growth of KH modes, nonlinear KH mode can still occur for the KH wave with a **k** vector tilted out of equatorial plane (Adamson et al., 2016; Grygorov et al., 2016).

For northward IMF conditions, nonlinear KH waves that are localized in the vicinity of the equatorial plane can twist the magnetic field, which drives pairs of high-latitude magnetic reconnection sites, transporting plasma by exchanging the part of magnetic flux tube between these two reconnection sites (Borgogno et al., 2015; Faganello et al., 2012; Leroy & Keppens, 2017; Otto, 2008). This process is sketched in Figure 1, showing a closed magnetospheric field line (black) and solar wind field line (red) before (left) and after (right) high-latitude double reconnection operates. The blue circles highlight the high-latitude reconnection sites. Note that the high-latitude reconnection sites are expected to be several Earth radii away from the equatorial plane and far from the cusp region. The resulting plasma transport process is highly dependent on the total amount of double-reconnected flux. In a highly symmetric configuration, reconnection at the northern and southern reconnection sites proceeds simultaneously, thereby capturing a section of a magnetosheath flux tube without the generation of open flux. However, in a realistic situation this symmetry is broken such that open flux is generated in addition to capturing magnetosheath flux tubes similar to high-latitude (cusp) reconnection for northward IMF. In principle, the symmetry of these two reconnection sites can be broken because of the asymmetric boundary conditions or with asymmetric perturbations, which reduces the total double-reconnected flux and consequently decreases the plasma transport efficiency. As such, it is important to identify the primary factors that control the total open and double-reconnected flux, and a tightly related question is to quantify the efficiency of this plasma transport process under typical magnetopause conditions at the Earth. This process is expected only for mostly northward IMF because for southward IMF a large section of the flank boundary including the equatorial region is subject to magnetic reconnection such that KH-mediated reconnection is not anymore confined to regions above and below the equatorial plane. Corresponding investigations for southward IMF have been conducted by Ma et al. (2014a, 2014b). This paper will address

Table 1
Normalization Units

Quantity	Value
Magnetic field B_0	16 nT
Number density n_0	11 cm^{-3}
Length scale L_0	600 km
Velocity V_A	105 km s^{-1}
Time t_0	5.7 s

these two questions by using three-dimensional MHD simulations for mostly northward IMF. The numerical model is introduced in section 2. The results, discussion, and summary are presented in sections 3–5, respectively.

2. Methods

2.1. Numerical Model

We use a leap frog scheme to numerically solve the full set of normalized resistive MHD equations (Potter, 1973; Birn, 1980; Otto, 1990), because this scheme has the advantage of second-order accuracy and low-numerical diffusion. All physical quantities are normalized to the typical value, that is, the length scale, L, to the half width of the initial sheared flow, L_0; density, ρ, to, $\rho_0 = n_0 m_0$, with the number density, n_0, and ion mass, m_0; the magnetic field, $\mathbf{B}$, to B_0; the velocities to the typical Alfvén speed, $V_A = B/\sqrt{\mu_0 \rho_0}$, with vacuum permeability, μ_0; the thermal pressure, p, to, $P_0 = B_0^2/(2\mu_0)$; and time, t, normalized to the Alfvén transit time, $t_0 = L_0/V_A$. The values for the normalization of the simulation units are summarized in Table 1.

The simulations are carried out in a rectangular domain $|x| \le L_x$, $|y| \le L_y$, and $|z| \le L_z$, which is resolved by 201 grid points along each direction (i.e., uniform along the y direction, and nonuniform along the x and z directions with the best resolution of $\Delta x = 0.15$, and $\Delta z = 0.2$ in the center); see Figure 2. The x direction is the normal direction of the sheared flow layer, the z direction points to the north, and the y direction is along the sheared flow direction, which is determined by the right-hand rule. Hence, the right half domain (i.e., $x > 0$) is referred to as Region 1 or the magnetosheath side, while the left half domain (i.e., $x < 0$) is referred to as Region 2 or the magnetospheric side. The upper half domain (i.e., $z > 0$) is referred to as the North Hemisphere, and the lower half domain (i.e., $z < 0$) is referred to as the South Hemisphere. The $z = 0$ plane is referred to as the equatorial plane. The simulation domain in the x direction, $L_x = 30$, is large enough such that boundary conditions in the x direction have minor influence on the simulation results. The simulation domain in the y direction, $L_y = 20$, corresponds to a typical KH wavelength in the magnetospheric flank region (i.e., 4 Earth radii) (Otto & Fairfield, 2000). It has been demonstrated that the size of the KH unstable region along the z direction, L_z, also limits the longest KH wavelength mode in the system (Ma et al., 2014a). In the real magnetopause, the size along the z direction is determined by the curvature of the magnetic field. As such, unstable KH waves have a wavelength limited by the size along the z direction, L_z, are expected. We run test simulations with different sizes of the simulation domain along the z direction and found that the KH growth rate saturates when $L_z \gtrsim 40$. Thus, in this study, the size of the simulation domain along the z direction, L_z, is set to be 40.

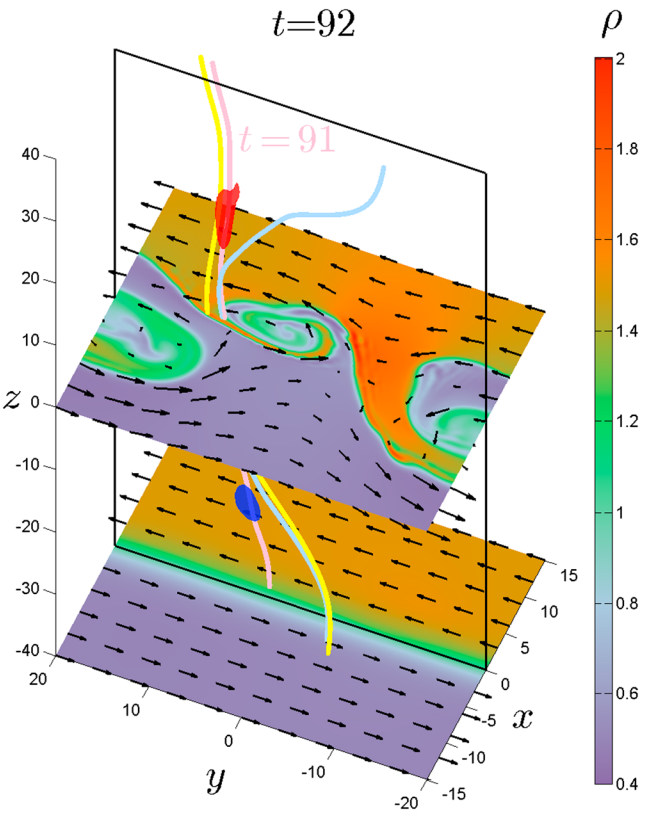

Figure 2. A perspective view of the selected magnetic field lines obtained at $t = 92$ for Case 1. The color index represents the plasma density, the black arrows indicate the in-plane bulk velocity, the red and blue patches are the isosurface of 0.85 max $E_{\parallel}$ and 0.85 min $E_{\parallel}$, respectively. The yellow line is an open field line at $t = 92$. The pink and blue lines are the traced field line at $t = 91$ and $t = 92$, respectively.

The KH instability is treated as an initial value problem. The initial steady state is a one-dimensional (1-D) transition layer. The sheared flow profile is given by $V_y = V_0 \tanh(x)$, where the magnitude of sheared flow, V_0, as a free parameter varies from 0.5 to 1. This implies that the simulation frame is roughly moving with the KH vortex rather than being fixed to the magnetosphere. The density profile is $\rho = \bar{\rho} + \delta\rho \tanh(x)$, where, $\bar{\rho} = \frac{1}{2}(\rho_1 + \rho_2)$ and $\delta\rho = \frac{1}{2}(\rho_1 - \rho_2)$. The y and z components of magnetic field are given by $\mathbf{B} = \bar{\mathbf{B}} + \delta\mathbf{B} \tanh(x)$, where vector $\bar{\mathbf{B}} = [B_y, B_z]$, $\bar{\mathbf{B}} = \frac{1}{2}(\mathbf{B}_1 + \mathbf{B}_2)$, $\delta\mathbf{B} = \frac{1}{2}(\mathbf{B}_1 - \mathbf{B}_2)$, and $\mathbf{B}_i = [B_i \sin\theta_i, B_i \cos\theta_i]$. Here the angle between the magnetic field and the z direction is θ; the subscript, $i = 1$ or 2, refers to Regions 1 and 2, respectively. The thermal pressure $p(x)$ is determined by the total pressure balance, $B^2 + p = \max(B_1, B_2)^2 + p_\infty$, where the thermal pressure on the magnetosheath side, p_∞, is set to be 1. The value of the free parameters for each case is listed in Table 2.

Our initial conditions are intrinsically KH unstable to a wide range of perturbations. A systematic approach to the properties of the KH instability is through eigenmodes (e.g., Chandrasekhar, 1961), but analytical solutions for compressible 3-D configurations with a finite width of the sheared flow are not available.

Table 2
Summary of Cases Used in This Study

Case number	ρ_1	ρ_2	B_1	B_2	θ_1	θ_2	j_c	Perturbation
1	1.5	0.5	1.2	0.8	5°	−5°	0.4	f_s
2	1.0	1.0	1.0	1.0	0°	0°	0.4	f_s
2.a	1.0	1.0	1.0	1.0	0°	0°	0.4	f_a
2.d	1.8	0.2	1.0	1.0	0°	0°	0.4	f_s
2.j	1.0	1.0	1.0	1.0	0°	0°	1.4	f_s
3	1.0	1.0	1.0	1.0	10°	−10°	0.4	f_s
3.d	1.8	0.2	1.0	1.0	10°	−10°	0.4	f_s
4	1.0	1.0	1.0	1.0	20°	−20°	0.4	f_s
4.d	1.8	0.2	1.0	1.0	20°	−20°	0.4	f_s
5	1.0	1.0	1.0	1.0	30°	−30°	0.4	f_s
5.a	1.0	1.0	1.0	1.0	30°	−30°	0.4	f_a
5.d	1.8	0.2	1.0	1.0	30°	−30°	0.4	f_s
5.j	1.0	1.0	1.0	1.0	30°	−30°	1.4	f_s

Note. Here ρ, B, and θ are plasma density, the magnitude of magnetic field, and angle between the magnetic field and the z direction, respectively. The subscript, $i = 1$ or 2, refers to Regions 1 and 2, respectively. The critical current density in the current-dependent resistivity model is j_c. The symmetric and asymmetric initial perturbation is labeled by f_s and f_a, respectively.

Nevertheless, such eigenmodes for long-wavelength conditions are expected to be close to the eigenmodes for incompressible 2-D configurations with an infinitely thin width of the sheared flow. Hence, the velocity perturbation is set to be $\delta\mathbf{v} = \delta v f(z)\nabla\Phi(x,y)\times\mathbf{e}_z$, where the amplitude of the perturbation, $\delta v = 0.025V_0$, the stream function is $\Phi = -k^{-1}\cosh^{-2}(x/2)\cos(ky)$, KH wave number, $k = \pi/L_y$, and the localization function along the z direction is $f(z,z1,z2) = 0.5\{\tanh[(z-z_1)/6] - \tanh[(z-z_2)/6]\}$. Here variables, z_1 and z_2, determine the width and location of the perturbation. To investigate the influence of the symmetrical properties of the initial perturbation, two types of the localization functions are applied in this study, that is, symmetrical localization $f_s(z) = f(z,-15,15)$, and asymmetrical localization $f_a(z) = f(z,0,15)$, (see Figure 3).

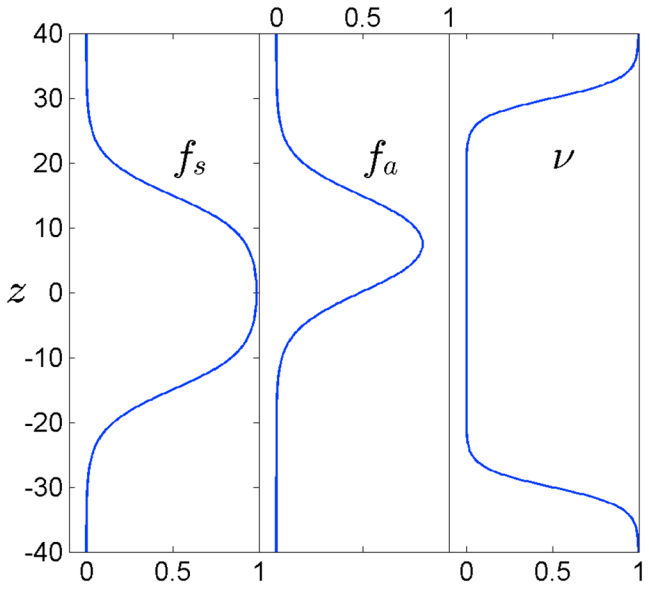

Figure 3. The symmetrical localization function, $f_s(z)$, the asymmetrical localization function, $f_a(z)$, and the friction coefficient, $\nu(z)$.

This study investigates the process where a nonlinear ideal instability (i.e., the KH instability) triggers a secondary nonideal evolution (i.e., the tearing mode or more precisely component magnetic reconnection), which requires the presence of nonzero resistivity only in the diffusion region. Hence, we applied a current-dependent resistivity model, which is given by $\eta(j) = \eta_0\sqrt{j^2 - j_c^2}H(j-j_c)+\eta_b$ (Nykyri & Otto, 2001, 2004; Ma et al., 2014a, 2014b). Here $H(x)$ is the Heaviside unit step function (Arfken et al., 2011), the critical current density, j_c, is set to be 0.4, and 1.4, the coefficient $\eta_0 = 0.2$, and background resistivity, η_b, is 0.002. As such, the resistivity is very small (i.e., 0.002) almost everywhere except in the location where the relative electron and ion drift speeds are large. High-latitude reconnection also occurs by using a constant resistivity model (Borgogno et al., 2015), suggesting that this process is insensitive to the resistivity model.

It is conventional to set periodic boundary conditions along the y direction. The boundary conditions along the x direction are given by $v_x = 0$, and $\partial_x = 0$ for other quantities. For the boundary conditions along the z direction, we add an artificial friction term, $-\nu(z)\rho(\mathbf{V} - \mathbf{V_0})$, on the right-hand side of the momentum equation, localized at the top and bottom boundaries to mimic the magnetic flux tube being carried by the fast tailward moving solar wind and to limit the KH unstable region along the z direction (Ma et al., 2014a; Ma, Otto, & Delamere, 2016). Here $\mathbf{V_0}$ is the initial sheared flow profile, and the

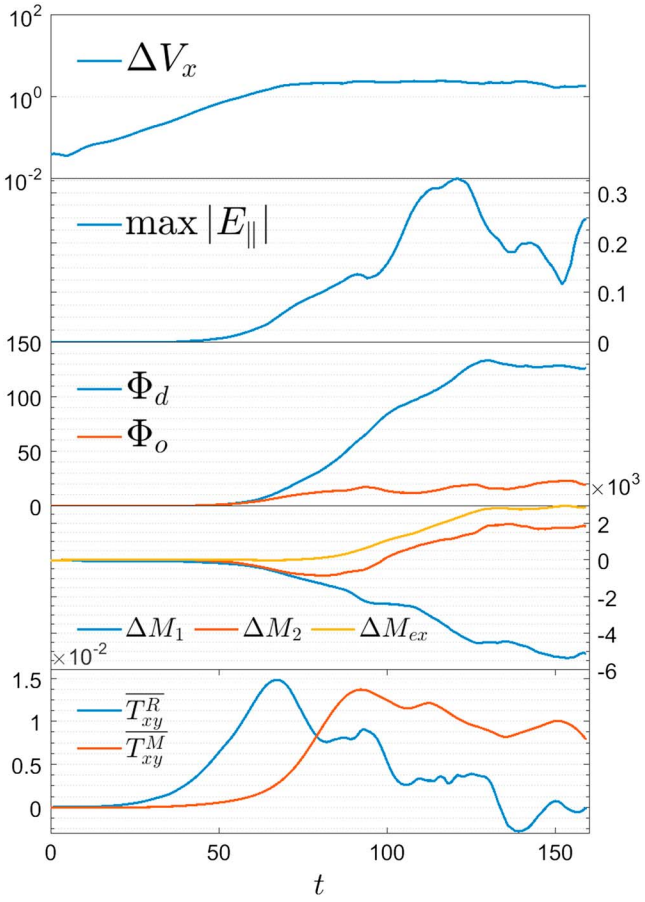

Figure 4. The overall dynamics of Case 1. From top to bottom: the growth of KH mode, the maximum parallel electric field, the open and double-reconnected flux, the change of mass on closed field line in Regions 1 and 2, and the normalized average of the *xy* component of the Maxwell and Reynolds stresses, respectively.

friction coefficient is given by $\nu(z) = 0.5\{2 - \tanh[(z + 30)/3] + \tanh[(z - 30)/3]\}$, (see Figure 3). This dissipation term damps the energy in the perturbation, maintaining the initial velocity profile. As such, the boundaries between magnetosheath and magnetospheric sides, (i.e., x=0), at top and bottom boundaries, do not move during the whole process.

In this study, for any given time, magnetic field lines can be traced by solving the ordinary differential equation, $d\mathbf{x}/d\tau = \mathbf{B}(\mathbf{x})$, from a specified starting point, $\mathbf{x}_0$, at $\tau = 0$, where $d\tau$ is an infinitesimal length along the magnetic field line, and $\mathbf{B}(\mathbf{x})$ is the magnetic field as a function of position, $\mathbf{x}$. Analogously, fluid parcels can be traced by solving the ordinary differential equation, $d\mathbf{x}/dt = \mathbf{V}(\mathbf{x})$, from a specified starting point, $\mathbf{x}_0$, at $t = 0$.

At the Earth's magnetopause, a closed magnetospheric field line means a magnetic field line traced from the Southern Hemisphere will eventually meet the ionosphere in the Northern Hemisphere. In contrast, an open field line means that a magnetic field line from either hemisphere does not reach the opposite hemisphere but extends into the magnetosheath. The same concept applies here, where $x < 0$ refers to the magnetosphere side, and $x > 0$ represents the magnetosheath side at the unperturbed top and bottom boundaries. If the footprints of the magnetic field at the top and bottom boundaries are on the same side of the magnetosphere-magnetosheath boundary (i.e., x =0), then this is a closed field line. In contrast, if the footprints of the magnetic field at top and bottom boundaries are on different sides of the magnetosphere-magnetosheath boundary (i.e., x=0), then it is an open field line. If at $t = t_1$ the top and bottom footprints of a field line are in Region 1, and at $t = t_2$ the footprints are in Region 2, then it is a double-reconnected field line.

3. Results

3.1. Overall Dynamics

Figure 4 shows central properties that represent the overall dynamics for Case 1. Linear theory implies exponential growth of the perturbations for an eigenmode (Chandrasekhar, 1961). As such, both the growth of the velocity V_x component and the magnetic B_x component can be employed to directly determine the growth of the KH mode. Other quantities require a separation of steady state and perturbation. However, the magnetic B_x component is strongly modified after the occurrence of magnetic reconnection. Therefore, the growth of the KH mode is chosen to be represented by the range of the velocity V_x component, $\Delta V_x = \max(V_x) - \min(V_x)$, in Figure 4 (first panel), showing that the nonlinear stage starts around $t = 70$. Figure 4 (second panel) shows the maximum parallel electric field, $\max |E_{\|}|$, indicating that reconnection operates at the end of the linear stage when the maximum current density is greater than the critical density.

The unperturbed top and bottom boundaries provide a well-defined boundary between the magnetosheath and the magnetospheric sides. Thus, the open and double-reconnected flux can be identified through the connectivity of magnetic lines. For instance, Figure 2 shows the plasma density (color index), and the in-plane bulk velocity (black arrows) in the equatorial and bottom planes during the nonlinear stage of Case 1 (t=92), indicating strong KH vorticities in the equatorial plane and an unperturbed bottom plane. The localized parallel electric field components (red and blue isosurfaces) indicate the higher-latitude reconnection sites. The upper footprint (i.e., the footprint in the top plane) of the yellow line is in Region 1 (i.e., $x > 0$), while the bottom footprint (i.e., the footprint in the bottom plane) is in Region 2 (i.e., $x < 0$), which is a typical open field line. In contrast, a selected fluid element originating in the equatorial plane on the magnetosheath side is traced in the simulations. The pink and blue lines are the magnetic field lines through this selected fluid element at $t = 91$ and $t = 92$, respectively. Note that the upper and bottom footprints of the pink line are in Region 1, which is typical of a magnetosheath closed field line. However, both footprints cross the boundary at $t = 92$ (i.e., blue line), implying that the magnetic flux frozen-in by this selected fluid element experienced double reconnection between t=91 and t=92.

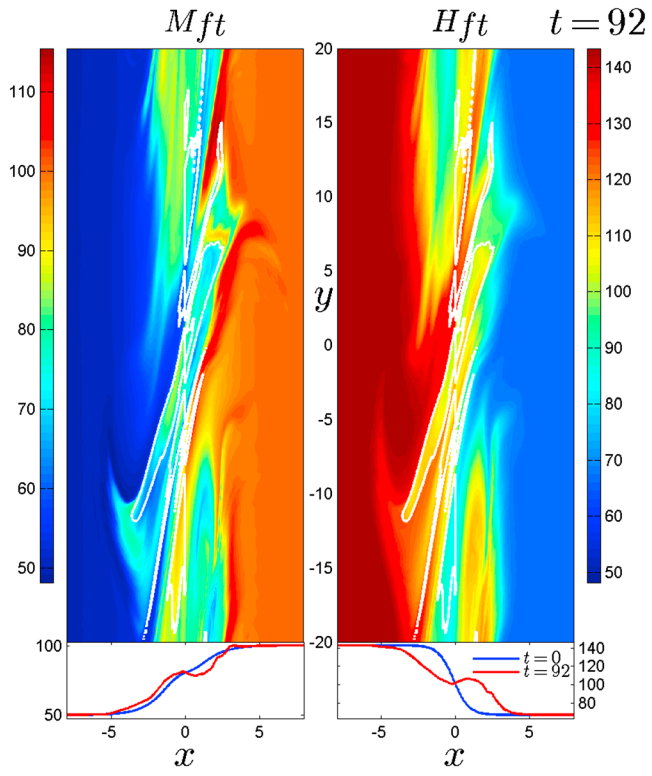

Figure 5. The flux tube mass (left) and flux tube entropy (right) of the traced magnetic field lines from the top boundary at $t=92$ (top) and their average values along the y direction at $t=0$ and 92 (bottom) for Case 1. The open-closed boundary is represented by the white line.

In this study, the total amount of open flux, Φ_o, is identified by tracing 1.6×10^5 magnetic field lines from the top boundary for each snapshot, which proved to be a sufficient number of field lines for this purpose. The same number of fluid elements initially in the equatorial plane are traced to identify the total amount of double-reconnected flux, Φ_d. The adequacy of the traced fluid elements is verified by comparing the total amount of open flux with the results obtained by tracing the field lines from the top boundary. Figure 4 (third panel) shows the total amount of open flux, Φ_o, and the total amount of double-reconnected flux, Φ_d. The total amount of double-reconnected flux rapidly increases after reconnection has turned on and eventually saturates at a high value of 145 after $t=130$. In contrast, the total amount of open flux slowly increases and saturates at a low value of 10, which is much smaller than the total amount of double-reconnected flux mainly because magnetic shear is small in Case 1 (i.e., $\theta_1=-\theta_2=5°$). It can be shown analytically that reconnection should occur symmetrically in the absence of magnetic shear. We will discuss the primary factors that control the total amount of open and double-reconnected flux in more detail in section 3.3.

It can be readily demonstrated that the flux tube mass, $M_{ft}=\int(\rho/B)d\tau$, and flux tube entropy, $H_{ft}=\int(p^{1/\gamma}/B)d\tau$, are conserved quantities, and the change of these quantities can be only due to the violation of the frozen-in condition through magnetic reconnection from the MHD perspective (Birn et al., 2006). Figure 5 (top) represents the flux tube mass (left), and flux tube entropy (right) of traced magnetic field lines from the top boundary at $t=92$ for Case 1, showing a fully mixed boundary layer due to flux tube exchange driven by the double reconnection process. Figure 5 (bottom) shows the spatial average over one wave period of these two quantities at $t=0$ and 92, indicating a signification diffusion (transport of mass and flux tube entropy) compared to the initial boundary layer.

For Case 1, there is a net mass transport from the magnetosheath side to the magnetospheric side. As such, the total amount of mass in the closed flux regions of the magnetosheath and magnetosphere can be defined as, $M_c=\int\int M_{ft}d\Phi_c$, where the integral is taken for the close field lines on the magnetosheath or magnetospheric sides. Figure 4 (fourth panel) shows the change of the total mass in the closed flux, $\Delta M(t)=M_c(t)-M_c(0)$, for both Region 1 (magnetosheath side) and Region 2 (magnetospheric side). The rapid increase of ΔM_2 and decrease of ΔM_1 are consistent with the fast increase of the double-reconnected flux, suggesting that the mass transport is mostly through the exchange of flux tubes. It is expected that ΔM_i eventually becomes saturated at the end of the simulation, when the nonlinear KH waves form a wide boundary layer.

Apparently, the mass loss on the magnetosheath side is greater than the mass gain on the magnetospheric side, because the change of the mass in the closed flux is due to the change of the mass through the reconnected flux tube exchange, as well as the loss of mass through the open flux. This also explains the loss of magnetospheric mass near $t=80$, when the total amount of open flux is relatively significant compared with the total amount of double-reconnected flux. In our simulation, the change of mass through the exchange of the flux tubes can be measured by integrating the change of the flux tube mass over the closed flux, $M_{ex}(t)=\int\int[M_{ft}(t)-M_{ft}(0)]d\Phi_c$. (The change of the flux tube mass for a closed flux tube without involving double reconnection is zero, i.e., $M_{ft}(t)-M_{ft}(0)=0$.) The yellow line in Figure 4 (fourth panel) shows that the total exchanged mass, M_{ex}, is a bit greater than the mass gain on the magnetospheric side, ΔM_2, being consistent with the mass loss through the open flux.

As a large-scale viscous-like process, the nonlinear KH instability also transports a significant amount of momentum through the boundary even without involving magnetic reconnection (Miura, 1984). In principle, the momentum transport can be described by the Maxwell stress, $\mathbf{T}^M=\mathbf{BB}$, and the Reynolds stress, $\mathbf{T}^R=-\rho\mathbf{VV}$, where the Reynolds stress depends on the reference frame (Miura, 1982, 1984). It is convenient to choose the magnetosphere as the rest frame. Figure 6 shows the xy component of the Maxwell stress, $T^M_{xy}=B_xB_y$, and the Reynolds stress, $T^R_{xy}=-\rho V_xV'_y$ in the $x=0$ plane at $t=92$ for Case 1, where $V'_y=V_y+V_0$ is the y component of

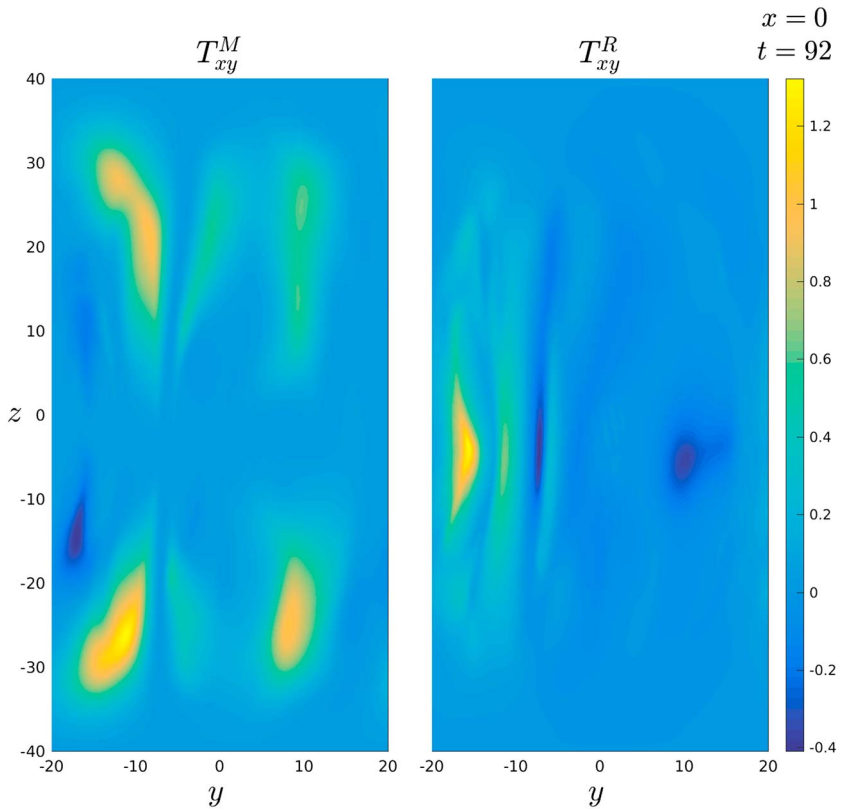

Figure 6. The *xy* component of the Maxwell (left) and Reynolds (right) stresses in the $x = 0$ plane at $t = 92$ for Case 1.

the velocity in the magnetospheric frame. The Reynolds stress with a wave-like structure is mostly localized at low latitudes, being consistent with the nonlinear KH waves. In contrast, the Maxwell stress is mainly located at high latitudes, where the magnetic field lines are dramatically bent.

Figure 4 (fifth panel) shows the spatial average of Maxwell, $\overline{T^M_{xy}}$, and Reynolds, $\overline{T^R_{xy}}$, stresses over the $x = 0$ plane, which are normalized by the magnetosheath dynamic pressure in the magnetospheric frame, $T_0 = 4\rho_1 V_0^2$. The Reynolds stress dominates in the linear stage with a peak value of $0.015T_0$ and becomes small and even negative, meaning a small reverse transport, during the nonlinear stage. In contrast, the Maxwell stress reaches its peak value of $0.015T_0$ in the early nonlinear stage (i.e., $t \approx 90$) and becomes saturated at a relatively large value of $0.008T_0$. This result suggests that the magnetic field lines, which cross the magnetosheath-magnetospheric boundary (i.e., $x = 0$), play the dominant role in dragging the solar wind and transport momentum from the solar wind into the magnetosphere (i.e., "viscous-interaction") (Burkholder et al., 2017).

3.2. Magnetic Reconnection and Parallel Electric Fields

Magnetic reconnection can be investigated through the change of magnetic field line connections, as well as through local physical quantities. The strong parallel electric field, $E_\parallel$, only exists in the vicinity of the diffusion region for 3-D magnetic reconnection. Figure 7 shows the integral of the parallel electric field along the *y* direction, $\phi_y = \int E_\parallel dy$, illustrating the localization of the parallel electric field at high latitudes (i.e., $z \sim \pm 30$). Meanwhile, the dynamic processes near the equatorial plane remain quasi 2-D. Thus, magnetic reconnection operates at low latitudes when a small magnetic field component along the sheared flow direction is present in the boundary configuration. In the next section, we will demonstrate that this configuration is north-south asymmetric. Figure 8 shows the localized strong parallel electric field (color index) at the edge of the vortex region and the region that connects the two neighboring vortices (hereafter referred to as the "spine region") close to the equatorial plane (i.e., $z = -4.6$), indicated by the in-plane magnetic field (white arrows), which is consistent with the 2-D simulation results (Otto & Fairfield, 2000; Nakamura et al., 2006, 2008).

General magnetic reconnection theory (Schindler et al., 1988) shows that for $\mathbf{B} \neq 0$ magnetic reconnection with global effects occurs if and only if the integral of the parallel electric field along the magnetic field line,

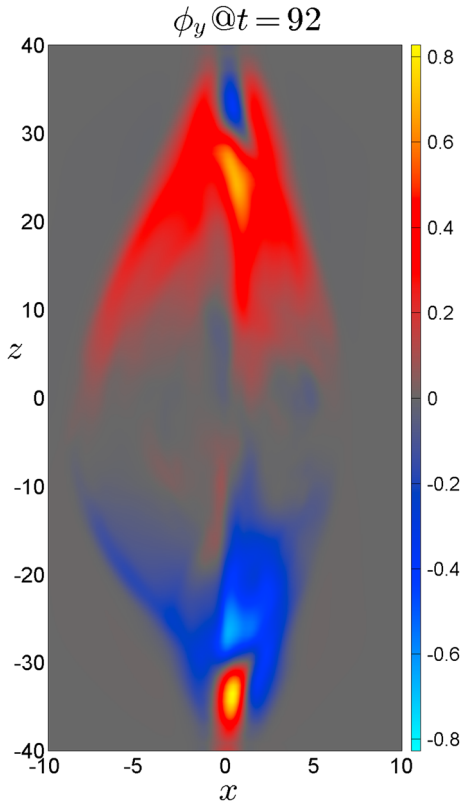

Figure 7. Integral of parallel electric field along the y direction at $t = 92$ for Case 1.

$\phi_r = \int E_\parallel d\tau$, (hereafter referred as the "residual potential") is nonzero on a measurable set of field lines in the diffusion region (Hesse & Schindler, 1988). For the 3-D geometry with a single reconnection site, the maximum value of the residual potential yields the same rate of reconnected flux (Hesse & Birn, 1993). Figure 9 shows the residual potential of the magnetic field lines traced from the top plane (color index). The open-closed boundary (i.e., green contour lines) are located in the region where the magnitude of residual potential is large, indicating that those flux tubes have been newly reconnected. In contrast, the large amount of open flux without significant residual potential (e.g., $-10 < y < 5$region) has likely been reconnected at a much earlier time. Meanwhile, closed flux with a strong residual potential (e.g., red and blue patches in the $y > 0$ region) can be caused by asynchronous double reconnection.

The parallel electric field, $E_\parallel$, is mostly antisymmetric along the z direction because of the relatively large-scale MHD symmetry, (see Figure 7). In a strictly north-south symmetric configuration, all high-latitude double reconnection operates simultaneously and there is no open flux, which yields double-reconnected flux with a zero residual potential. However, the integral of the magnitude of the parallel electric field along those magnetic field lines (and hereafter referred as the "total potential"), $\phi_t = \int |E_\parallel| d\tau$, can be large. Figure 10 shows the total potential, ϕ_t, on the field lines traced from the top plane (color index), where the large total potential is mostly associated with double-reconnected flux. This is also confirmed by comparison with Figure 9 where the maximum magnitude of the residual potential is slightly less than half of the total potential, implying that field lines with large total potential have multiple contributions from reconnection regions with different signs of $E_\parallel$ relative to the magnetic field direction.

As we will discuss in section 4, the descriptions of reconnection from connectivity of magnetic lines aspects and parallel electric field aspects are not equivalent. The purpose of this study is to quantify the transport process, which is directly associated with connectivity of magnetic lines. The reconnected flux in this paper is therefore quantified via the connectivity of magnetic lines.

3.3. Magnetic Shear and Reconnected Flux

The presence of open flux is an indication of the asymmetry of high-latitude reconnection, which motives us to understand the local mirroring symmetry of the MHD equations (Otto et al., 2007). In order to maintain the symmetry of the MHD system along the z direction in the configuration with a nonzero magnetic field B_z component, and nonzero bulk velocity V_y, and V_x components, these three variables, and all positive definite variables (e.g., the plasma density), must be symmetric along the z direction, and the plasma bulk velocity V_z component, and the magnetic field B_x, and B_y components must be antisymmetric along the z direction (Otto et al., 2007). As such, the sheath-sphere asymmetric plasma density, pressure, and magnetic field B_z component cannot break the symmetry along the z direction. However, the presence of the magnetic field component along the sheared flow direction, i.e., B_y, in the initial 1-D steady state profile will cause the north-south asymmetry.

Cases 2, 3, 4, and 5 have a symmetric density (along the x direction) and symmetric initial perturbation (along the z direction), but with an antiparallel magnetic B_y component, i.e., $\theta_1 = -\theta_2 = [0, 10, 20, 30]$. The case with no magnetic shear (i.e., Case 2) is an ideally symmetric case, which serves as the reference case.

The solid lines in Figure 11 represent the results from Cases 2, 3, 4, and 5. Figure 11 (first panel) is the double-reconnected flux, Φ_d, showing that a large amount of magnetic flux is exchanged by the high-latitude double reconnection process in the symmetric case (Case 1, purple line). However, the presence of a magnetic B_y component significantly decreases the double-reconnected flux. In contrast, Figure 11 (second panel) shows the open flux, Φ_o. Note the different scales for the open (second panel) and double (first panel) reconnected flux. This shows that the open flux increases and saturates with increasing magnetic shear. This is because (a) the total flux through the top plane (i.e., $B_z = B\cos\theta$) decreases with the increase of the magnetic shear, (b) the magnetic $B_y = B\sin\theta$ component, which has the stabilization effect on the KH instability, increases with the increase of magnetic shear. The reason (b) is consistent with Figure 11 (third panel), showing that the half width of the total reconnected flux, $L_r = \Phi_r/(2L_yB_z)$, decreases with increasing magnetic shear. Here the half width of the total reconnected flux is normalized by the magnetic B_z component and the dimension along the y direction, $2L_y$, which somewhat represents the half width of the boundary generated by the KH instability. Figure 11 (fourth panel) shows the ratio of the open to the total reconnected flux, Φ_o/Φ_r during

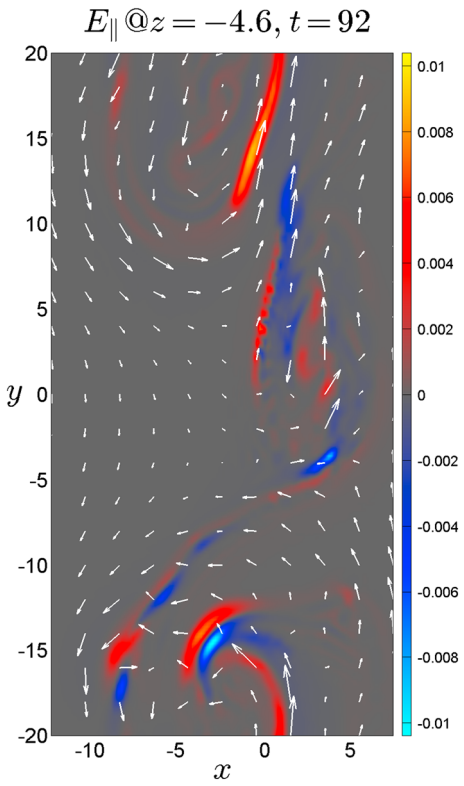

Figure 8. The parallel electric field (color index) and in-plane magnetic field (white arrows) in the $z = -4.6$ plane at $t = 92$ for Case 1.

the nonlinear stage, where the total reconnected flux $\Phi_r = \Phi_o + \Phi_d$. For the symmetric case (i.e., Case 2), the open flux is mostly caused by the numerical background noise, and it is indeed negligible compared to the total reconnected flux, i.e., about 5 % (purple line). For other cases, the ratio, $\Phi_o/\Phi_r = 1$, at the beginning of the nonlinear stage ($t \approx 40$), indicating that those processes generate open flux before the double-reconnected flux. This sequence is not important for the overall dynamics, because the amount of open flux is tiny (see second panel), and the ratio, Φ_o/Φ_r, eventually saturates. Figure 11 (fourth panel) shows that the proportion of open flux increases with the increase of the magnetic shear; however, except for Case 5 (i.e., $\theta_1 = 30$), the double-reconnected flux still dominates the total reconnected flux.

A north-south asymmetry can also be caused by background turbulence, which is somewhat represented by the numerical noise from the MHD simulations (e.g., Case 2). Especially, the current-dependent resistivity model is expected to amplify the asymmetry, which is examined in Cases 2.j and 5.j. We also include an asymmetric initial perturbation to increase the north-south asymmetry (i.e., Cases 2.a and 5.a).

Cases 2.a and 5.a are similar to Cases 2 and 5, respectively, except for using an asymmetric initial perturbation, which are represented by purple and orange dashed lines in Figure 11 (fourth panel). It suggests that an asymmetric initial perturbation (or a large background noise) may generate relatively more open flux for zero magnetic shear case (purple dashed line). However, the influence from the initial perturbation is negligible for the cases with a large magnetic shear (orange dashed line). This is expected, because the KH instability is indeed a boundary value problem rather than an initial value problem, which means that the overall dynamics, especially during the nonlinear stage, are mostly determined by the magnetospheric and magnetosheath conditions instead of the upstream perturbation.

Cases 2.d and 5.d are represented by the dashed dots lines in Figure 11 (fourth panel) and are similar to Cases 2 and 5, respectively, except for using a large sheath-sphere density asymmetry ($\rho_1/\rho_2 = 9$). It shows that the presence of the sheath-sphere density asymmetry in a south-north symmetric configuration cannot generate open flux (purple dashed dots line). Although the sheath-sphere density asymmetry increases the proportion of open flux for the cases with a large magnetic shear, the difference is relatively tiny (orange dashed dots line).

The dotted lines represent the cases (i.e., CaseS 2.j and 5.j) with a higher critical current density ($j_c = 1.4$) in the resistivity model, which requires magnetic reconnection to operate in a thinner current density layer (or reconnection diffusion width). The almost identical results between 2.j and 2, and 5.j and 5 suggest that the overall reconnected flux is mostly determined by the KH wave (or sheath-sphere conditions) rather than the specific detail of the reconnection diffusion region once reconnection operates.

3.4. Diffusion Coefficient

The KH instability is often considered as a diffusion process, which widens the boundary layer and mixes the plasma. Therefore, it is important to quantify the analogous diffusion coefficients whose dimension is area per unit time. As we have shown, the KH instability transports or mixes the flux, mass, and momentum. Thus, the diffusion coefficients associated with different physical transport processes are sometimes measured with different methods, and their values can be different.

Based on the momentum transport process, Miura (1984) suggested that the diffusion coefficient (or "anomalous viscosity") in an MHD fluid can be defined as

$$\nu_{\text{ano}} = \frac{\bar{T}^M_{xy} + \bar{T}^R_{xy}}{\rho_1 \mathrm{d}\overline{V'_y}/\mathrm{d}x}.$$

Here $\overline{V'_y}$ is the spatial average of the velocity V_y component over one wave period in the magnetosphere frame.

Figure 12 (first panel) shows the peak values of the spatial average of the Maxwell stress, $\bar{T}^M_{xy}$, and the Reynolds stress, $\bar{T}^R_{xy}$, over one wave period as a function of magnetic shear angles for the symmetric and asymmetric density cases (Cases 2–5 and 2.d–5.d), in units of the magnetosheath dynamic pressure, T_0. For the symmetric case, the Maxwell stress is about several percent of the magnetosheath dynamic pressure, which is on the same order of magnitude of the results by Miura (1984). The Reynolds stress is about half of the

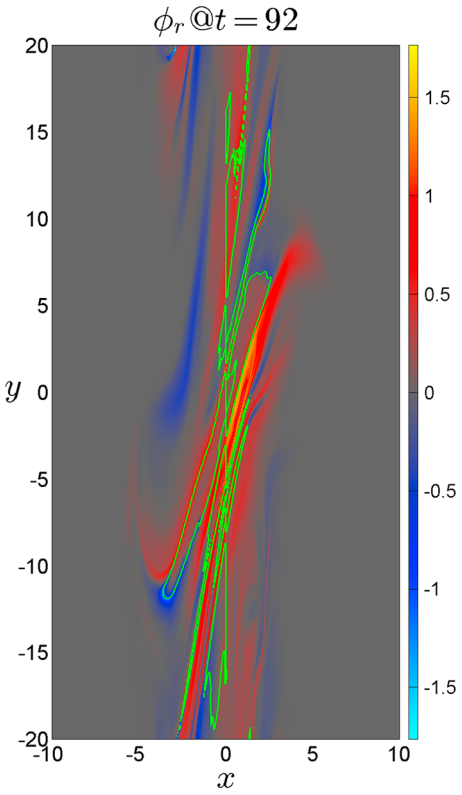

Figure 9. The residual potential of the traced magnetic field lines from the top boundary at $t = 92$ for Case 1. The open-closed boundary is represented by the green line.

Maxwell stress. The presence of a density asymmetry decreases the KH onset condition and consequently decreases the stresses. Figure 12 (second panel) shows the anomalous viscosity, which has a similar tendency as the stresses. The diffusion coefficient is about 0.1 in our normalization unit (i.e., $0.06aV_0$ in Miura, 1984, unit), which is about 4 times greater than the 2-D results. For typical Earth-like parameters, this yields a diffusion coefficient of 6×10^9 m^2 s^{-1}, which is consistent with the value suggested by Sonnerup (1980).

In hybrid simulations, Cowee et al. (2009, 2010) suggested that the diffusion coefficient is determined by the mean square perpendicular displacement of particles over time. Equivalently, Delamere et al. (2011) used the time derivative of the square of the width of the mixing region, where mixed cells contain between 25% and 75% of ions that were initialized on a given side of the sheared flow boundary. For MHD simulations, the mixing region cannot be determined by the source of the particles. However, plasma mixes when reconnection connects magnetic flux from different regions. As such, the width of the total reconnected flux is equivalent to the width of the mixing region suggested by Delamere et al. (2011), and the diffusion coefficient can be defined as

$$D_{\mathrm{mix}} = \frac{4\mathrm{d}L_r^2}{\mathrm{d}t}.$$

Figure 12 (third panel) shows the peak value of the diffusion coefficient associated with reconnected flux, D_{mix}, as the function of magnetic shear angle for both symmetric and asymmetric cases. The results suggest that the diffusion coefficient ranges from 0.6 to 2.2, (i.e., $2.8–14 \times 10^{10}$ m^2 s^{-1}), being one order of magnitude greater than the 2-D results by Cowee et al. (2009, 2010) and Delamere et al. (2011).

The diffusion coefficient also can be measured through the net mass transport in a density asymmetric condition. Nykyri and Otto (2001, 2004) suggested that an average entry velocity is given by

$$V_e = \frac{\mathrm{d}M}{\mathrm{d}t}\frac{1}{2L_y\rho_1},$$

where M is the mass of the magnetic island in 2-D, and the equivalent diffusion coefficient, (i.e., $D_{\mathrm{ent}} = V_e L$) assuming a boundary layer width of $L = 10 \times 10^3$ km. As such, for 3-D, the equivalent diffusion coefficient can be defined as

$$D_{\mathrm{ent}} = \frac{\mathrm{d}M_{ex}}{\mathrm{d}t}\frac{1}{2L_y\rho_1}.$$

Figure 12 (bottom) shows the peak value of the diffusion coefficient based on the exchange of plasma, D_{ent}, as a function of magnetic shear angle, which is very close to the diffusion coefficient associated with reconnected flux, D_{mix}.

4. Discussion

The transport process driven by the KH instability is highly dependent on the growth of the KH instability, and consequently sensitive to the direction of the KH wave vector. In our simulations, the localized KH wave along the z direction indicates a z component of the KH wave vector. As such, the KH growth rates for the conditions with antiparallel magnetic B_y components are smaller than they were for the conditions with parallel magnetic B_y components. The difference can be significant for a large magnitude of the magnetic B_y component. Here we only investigated the case with antiparallel magnetic B_y components. The case with parallel magnetic B_y components can be converted to the case with no magnetic B_y component (however, with a flow shear along the z direction) by rotating the coordinates, which is beyond the scope of this paper. At the magnetopause, the KH instability is expected to operate along the most unstable direction, which can be easily deduced from linear theory (Adamson et al., 2016).

In the 2-D configuration, the presence of the antiparallel magnetic B_y components in the initial configuration can trigger so called "type-I reconnection" (Nakamura et al., 2008). This type of reconnection operates when

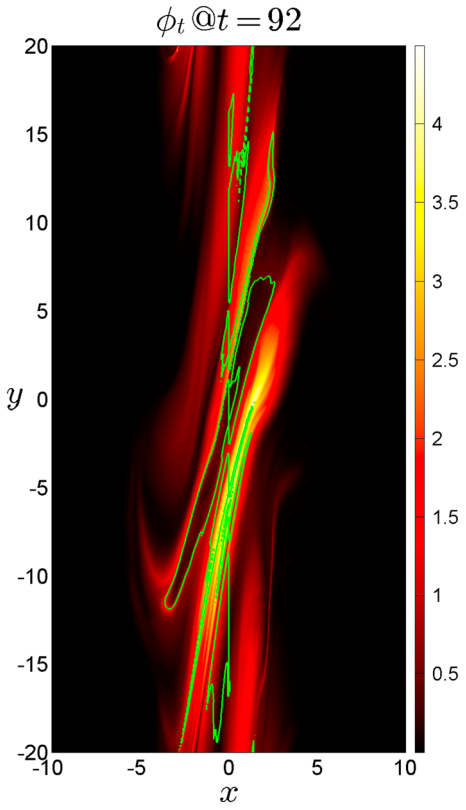

Figure 10. The total potential of the traced magnetic field lines from the top boundary at $t = 92$ for Case 1. The open-closed boundary is represented by the green line.

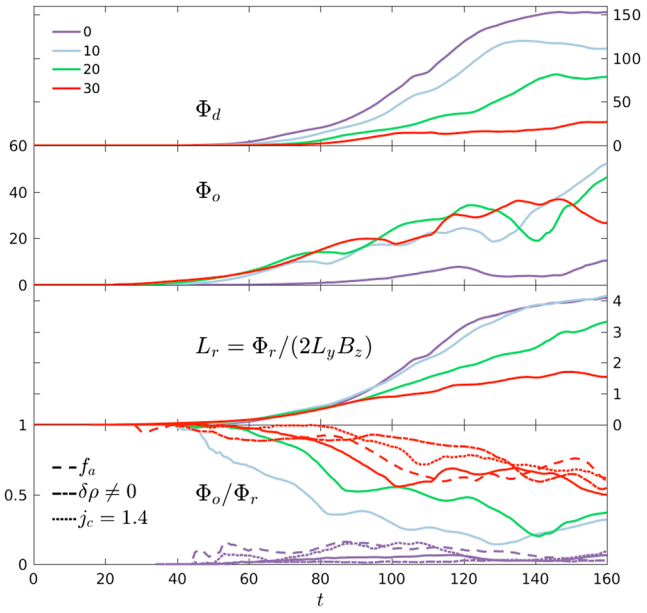

Figure 11. From top to bottom: The double-reconnected flux, the open flux, half width of the total reconnected flux, and the ratio of open to the total reconnected flux vary with different magnetic tilt angles.

the initial current layer (i.e., the gradient of the magnetic B_y component) in the KH spine region is compressed by the nonlinear KH waves. As such, type-I reconnection connects the magnetosheath flux with the magnetospheric flux, i.e., the open flux. In contrast, parallel magnetic B_y components in the initial configuration can cause so called "type-II reconnection" (Nakamura et al., 2008), which only operates when the KH vortex completely twists the in-plane magnetic field lines, forming antiparallel magnetic field components. As such, magnetic reconnection actually operates on the same field line, which generates magnetic islands and associated plasma transport. However, the actual plasma transport in 3-D and the question of whether magnetic flux is open or closed cannot truly be resolved in two dimensions and requires three-dimensional studies.

In principle, magnetic reconnection can be described (or defined) from the connectivity of magnetic field lines and local physical (i.e., parallel electric field) aspects. In some idealized situations, these two aspects can be equivalent. For instance, in a strictly north-south symmetric configuration, all high-latitude double reconnection operate simultaneously and there is no open flux. As such, the double-reconnected flux is associated with a large total potential and a tiny (or strictly zero) residual potential. The maximum of total potential can presumably represent the reconnection rate of simultaneous high-latitude double reconnection. However, the presence of north-south asymmetry is expected to generate an asymmetry in the high-latitude reconnection and thus a nonzero residual potential and net open flux. A newly opened flux tube can be generated by single reconnection at low-latitude, high-latitude single reconnection, or simultaneous double reconnection for an already open flux tube. The formation of double-reconnected flux can be both simultaneous and asynchronous. On the other hand, a closed flux tube (from the connectivity of magnetic lines perspective) can be caused by twice double reconnection or reconnection between the flux from the same sides of the boundary (e.g., type-II reconnection in 2-D configuration (Nakamura et al., 2008; Otto & Fairfield, 2000)).

The relation to the theory of general magnetic reconnection (Hesse & Schindler, 1988) is complicated because of the presence of multiple reconnection sites in our system. In a sufficiently simple system with one reconnection site, the total 3-D reconnection rate is determined by the maximum of the field-aligned integrated parallel electric field (here termed residual potential). However, in the presence of several reconnection regions this is not anymore valid. In fact, in an exactly symmetric system the reconnection rate as defined by general magnetic reconnection is zero. General reconnection assumes that reconnection indeed changes the connection of magnetic field lines. But this is not the case for "double reconnection" because a field line with a particular footprint location in the Northern Hemisphere which is originally connected to some footprint in the Southern Hemisphere remains connected to this point after double reconnection. So would this imply that this type of reconnective flux tube exchange should not be addressed as magnetic reconnection? We believe that this would be misleading based on two arguments: First, high-latitude reconnection is fast in our simulation (close to the Petschek rate, see max $|E_{\parallel}|$ in Figure 4). Second, when half of the system is considered (e.g., north), the reconnection at the northern boundary of the wave would be consistent with general magnetic reconnection since the physics at this northern side is mostly independent of the presence of a southern reconnection site.

Mass transport via the exchange of magnetic flux tubes implies that the direction of the transport is against the gradient of density per magnetic field rather

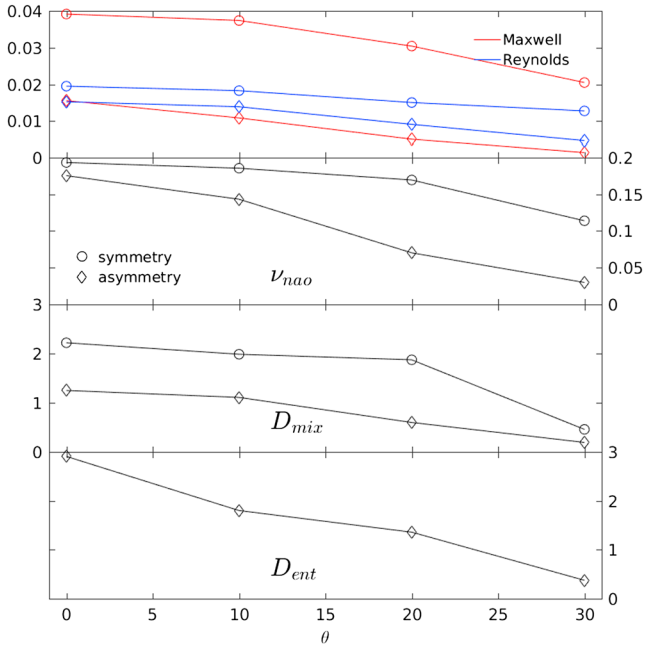

Figure 12. The peak value of the average of the Maxwell and the Reynolds stresses that are normalized by the magnetosheath dynamic pressure, T_0, (top), the anomalous viscosity, ν_{ano} (second), diffusion coefficient, D_{mix} (third), and D_{ent} (bottom) for different magnetic shear. The circles represent the symmetric density case, while diamonds represent the asymmetric density case.

than density alone. For the Earth, the magnetosheath plasma density is often one order of magnitude greater than the magnetospheric plasma density, while the magnitude of the magnetic field on both sides is comparable. Thus, there is always a net mass transport from magnetosheath to magnetosphere, unless the magnetosphere is influenced by the plasma plume (Walsh et al., 2015). For the giant planets, the plasma mass density per magnetic flux on the magnetosheath and magnetosphere sides is comparable, which potentially can transport the internal plasma source into the solar wind.

Flux tube entropy can be transported when the magnitude of magnetic field in the magnetosheath and magnetosphere are different. Magnetosheath plasma is much colder than magnetospheric plasma. Therefore, the exchange of flux tubes can dramatically reduce the magnetospheric flux tube entropy. These low entropy flux tubes are expected to move radially into the magnetosphere due to stability requirements (Birn et al., 2009). This process is akin to the interaction between the Kelvin-Helmholtz and the Rayleigh-Taylor instability, which is potentially important for the coupling between the solar wind and the magnetosphere and deserves further investigation.

The diffusion coefficient has been measured with three different methods. The anomalous viscosity, ν_{ano}, represents the transport of momentum, which is based on the Reynolds and Maxwell stresses (Miura, 1984). The diffusion coefficient, D_{mix}, which is based on the width of the mixing region, is somewhat equivalent to the diffusion coefficient defined in hybrid simulations (Cowee et al., 2009, 2010; Delamere et al., 2011). The diffusion coefficient, D_{den}, quantifies the efficiency of plasma transport via flux tube exchange process through high-latitude double reconnection, which is somewhat equivalent to the diffusion coefficient defined in 2-D MHD simulations (Nykyri & Otto, 2001). All three of those parameters in a 3-D configuration are greater than they are in a 2-D configuration and consistently show a decrease with a reduced KH growth rate. The anomalous viscosity is about one order of magnitude smaller than the other two diffusion coefficients. This could be partially because the measurement of anomalous viscosity is based on the average of the whole simulation domain, including the high-latitude KH stable region. Note that anomalous viscosity and a diffusion coefficient based on the reconnected flux can be determined for both north and southward IMF conditions. In contrast, the diffusion coefficient associated with flux tube exchange is only available under northward IMF conditions with an asymmetric density per magnetic field.

The concept of high-latitude reconnection driven by the nonlinear KH instability has been proposed a decade ago (Otto, 2008). However, until recently, there were only few studies trying to look for the in situ observational signature of this process (Vernisse et al., 2016). We will compare the observational data and numerical simulation in our next study. The KH instability is expected to play a more important role for the interaction between the solar wind and giant magnetospheres (i.e., Jupiter's and Saturn's magnetospheres), due to the fast rotational magnetodisc. The combination of rotational magnetosphere plasma and tailward solar wind flow causes a large sheared flow on the dawnside, which triggers rapidly growing KH instability and rapidly diffuses the boundary. As such, in situ observation can hardly identify clear observational signatures of KH waves (Ma et al., 2015). In contrast, KH waves originating from the subsolar point stop further evolution while they are advected to the duskside by the net tailward flow due to the lack of sheared flow. However, the preserved boundary modulation by the KH wave can be relatively easily identified through the in situ observational magnetic data (Delamere et al., 2013; Masters et al., 2009). This large-scale dawn-dusk KH instability asymmetry is expected to cause a dawn-dusk momentum transport asymmetry, which is recently confirmed by the Cassini Plasma Spectrometer data (Burkholder et al., 2017).

5. Summary

In this study we quantitatively analyzed the transport process driven by the KH instability under northward IMF conditions. Both the plasma and the flux tube entropy can be transported via a flux tube exchange process driven by high-latitude double reconnection. Such a double reconnection process can be simultaneous

as well as asynchronous. The presence of magnetic shear along the shear flow direction breaks south-north symmetry, which generates more open flux. A large magnetic shear decreases the KH growth rate and increases the portion of open flux, which significantly reduces the plasma and the flux tube entropy transport efficiency. For a well-developed nonlinear KH wave at Earth's magnetopause, the anomalous viscosity is about 6×10^9 m^2 s^{-1}, consistent with the value suggested by Sonnerup (1980). In contrast, the diffusion coefficient is greater than 1×10^{10} m^2 s^{-1}, which is one order of magnitude greater than the results from the 2-D geometry.

Acknowledgments
The authors acknowledge support from NASA grants NNX15AH09G and NNX13AH30G. The simulation data in this paper can be accessed from the corresponding author at xma2@alaska.edu. We are grateful to the International Space Science Institute (ISSI) for their support to the Coordinated Numerical Modeling of the Global Jovian and Saturnian Systems team. X.M. acknowledges Mr. Yixin Hao, Mr. Yajie Cao, Ms. Ram, and Ms. Rem for the suggestion on the color scheme.

References

Adamson, E., Nykyri, K., & Otto, A. (2016). The Kelvin-Helmholtz instability under Parker-spiral interplanetary magnetic field conditions at the magnetospheric flanks. *Advances in Space Research*, *58*(2), 218–230. https://doi.org/10.1016/j.asr.2015.09.013, Plasma Transport Across Magnetospheric Boundaries.

Arfken, G., Weber, H., & Harris, F. (2011). *Mathematical Methods for Physicists: A Comprehensive Guide*. New York: Elsevier.

Axford, W. I. (1964). Viscous interaction between the solar wind and the Earth's magnetosphere. *Planetary and Space Science*, *12*, 45–53.

Birn, J. (1980). Computer studies of the dynamic evolution of the geomagnetic tail. *Journal of Geophysical Research*, *85*, 1214–1222. https://doi.org/10.1029/JA085iA03p01214

Birn, J., Hesse, M., & Schindler, K. (2006). Entropy conservation in simulations of magnetic reconnection. *Physics of Plasmas*, *13*(9), 92117. https://doi.org/10.1063/1.2349440

Birn, J., Hesse, M., Schindler, K., & Zaharia, S. (2009). Role of entropy in magnetotail dynamics. *Journal of Geophysical Research*, *114*, A00D03. https://doi.org/10.1029/2008JA014015

Borgogno, D., Califano, F., Faganello, M., & Pegoraro, F. (2015). Double-reconnected magnetic structures driven by Kelvin-Helmholtz vortices at the Earth's magnetosphere. *Physics of Plasmas*, *22*(3), 32301. https://doi.org/10.1063/1.4913578

Burkholder, B., Delamere, P. A., Ma, X., Thomsen, M. F., Wilson, R. J., & Bagenal, F. (2017). Local time asymmetry of Saturn's magnetosheath flows. *Geophysical Research Letters*, *44*, 5877–5883. https://doi.org/10.1002/2017GL073031

Chandrasekhar, S. (1961). *Hydrodynamic and Hydromagnetic Stability*. The International Series of Monographs on Physics, Dover Publ.

Chen, Q. (1997). Two- and three-dimensional study of the Kelvin-Helmholtz instability, magnetic reconnection and their mutual interaction at the magnetospheric boundary (PhD thesis), University Of Alaska Fairbanks, Fairbanks.

Chen, Q., Otto, A., & Lee, L. C. (1997). Tearing instability, Kelvin-Helmholtz instability, and magnetic reconnection. *Journal of Geophysical Research*, *102*, 151–162. https://doi.org/10.1029/96JA03144

Chen, S.-H., & Kivelson, M. G. (1993). On nonsinusoidal waves at the Earth's magnetopause. *Geophysical Research Letters*, *20*, 2699–2702. https://doi.org/10.1029/93GL02622

Cowee, M. M., Winske, D., & Gary, S. P. (2009). Two-dimensional hybrid simulations of superdiffusion at the magnetopause driven by Kelvin-Helmholtz instability. *Journal of Geophysical Research*, *114*, A10209. https://doi.org/10.1029/2009JA014222

Cowee, M. M., Winske, D., & Gary, S. P. (2010). Hybrid simulations of plasma transport by Kelvin-Helmholtz instability at the magnetopause: Density variations and magnetic shear. *Journal of Geophysical Research*, *115*, A06214. https://doi.org/10.1029/2009JA015011

Delamere, P. A., Wilson, R. J., & Masters, A. (2011). Kelvin-Helmholtz instability at Saturn's magnetopause: Hybrid simulations. *Journal of Geophysical Research*, *116*, A10222. https://doi.org/10.1029/2011JA016724

Delamere, P. A., Wilson, R. J., Eriksson, S., & Bagenal, F. (2013). Magnetic signatures of Kelvin-Helmholtz vortices on Saturn's magnetopause: Global survey. *Journal of Geophysical Research: Space Physics*, *118*, 393–404. https://doi.org/10.1029/2012JA018197

Eriksson, S., Lavraud, B., Wilder, F. D., Stawarz, J. E., Giles, B. L., Burch, J. L., … Goodrich, K. A. (2016). Magnetospheric multiscale observations of magnetic reconnection associated with Kelvin-Helmholtz waves. *Geophysical Research Letters*, *43*, 5606–5615. https://doi.org/10.1002/2016GL068783

Faganello, M., Califano, F., Pegoraro, F., Andreussi, T., & Benkadda, S. (2012). Magnetic reconnection and Kelvin-Helmholtz instabilities at the Earth's magnetopause. *Plasma Physics and Controlled Fusion*, *54*(12), 124037.

Fairfield, D. H., Otto, A., Mukai, T., Kokubun, S., Lepping, R. P., Steinberg, J. T., … Yamamoto, T. (2000). Geotail observations of the Kelvin-Helmholtz instability at the equatorial magnetotail boundary for parallel northward fields. *Journal of Geophysical Research*, *105*, 21,159–21,174. https://doi.org/10.1029/1999JA000316

Grygorov, K., Němeček, Z., Šafránková, J., Přech, L., Pi, G., & Shue, J.-H. (2016). Kelvin-Helmholtz wave at the subsolar magnetopause boundary layer under radial IMF. *Journal of Geophysical Research: Space Physics*, *121*, 9863–9879. https://doi.org/10.1002/2016JA023068

Guo, X. C., Wang, C., & Hu, Y. Q. (2010). Global MHD simulation of the Kelvin-Helmholtz instability at the magnetopause for northward interplanetary magnetic field. *Journal of Geophysical Research*, *115*, A10218. https://doi.org/10.1029/2009JA015193

Hasegawa, H., Fujimoto, M., Phan, T.-D., Rème, H., Balogh, A., Dunlop, M. W., … TanDokoro, R. (2004). Transport of solar wind into Earth's magnetosphere through rolled-up Kelvin-Helmholtz vortices. *Nature*, *430*, 755–758. https://doi.org/10.1038/nature02799

Hasegawa, H., Fujimoto, M., Takagi, K., Saito, Y., Mukai, T., & RèMe, H. (2006). Single-spacecraft detection of rolled-up Kelvin-Helmholtz vortices at the flank magnetopause. *Journal of Geophysical Research*, *111*, A09203. https://doi.org/10.1029/2006JA011728

Hesse, M., & Birn, J. (1993). Parallel electric fields as acceleration mechanisms in three-dimensional magnetic reconnection. *Advances in Space Research*, *13*, 249–252. https://doi.org/10.1016/0273-1177(93)90341-8

Hesse, M., & Schindler, K. (1988). A theoretical foundation of general magnetic reconnection. *Journal of Geophysical Research*, *93*, 5559–5567. https://doi.org/10.1029/JA093iA06p05559

Hwang, K.-J., Kuznetsova, M. M., Sahraoui, F., Goldstein, M. L., Lee, E., & Parks, G. K. (2011). Kelvin-Helmholtz waves under southward interplanetary magnetic field. *Journal of Geophysical Research*, *116*, A08210. https://doi.org/10.1029/2011JA016596

Hwang, K.-J., Goldstein, M. L., Kuznetsova, M. M., Wang, Y., ViñAs, A. F., & Sibeck, D. G. (2012). The first in situ observation of Kelvin-Helmholtz waves at high-latitude magnetopause during strongly dawnward interplanetary magnetic field conditions. *Journal of Geophysical Research*, *117*, A08233. https://doi.org/10.1029/2011JA017256

Johnson, J., Wing, S., & Delamere, P. (2014). Kelvin Helmholtz instability in planetary magnetospheres. *Space Science Reviews*, *184*(1–4), 1–31. https://doi.org/10.1007/s11214-014-0085-z

Kavosi, S., & Raeder, J. (2015). Ubiquity of Kelvin-Helmholtz waves at Earth's magnetopause. *Nature Communications*, *6*, 7019. https://doi.org/10.1038/ncomms8019

Leroy, M. H. J., & Keppens, R. (2017). On the influence of environmental parameters on mixing and reconnection caused by the Kelvin-Helmholtz instability at the magnetopause. *Physics of Plasmas*, *24*(1), 12906. https://doi.org/10.1063/1.4974758

Li, W., André, M., Khotyaintsev, Y. V., Vaivads, A., Graham, D. B., Toledo-Redondo, S., … Strangeway, J. (2016). Kinetic evidence of magnetic reconnection due to Kelvin-Helmholtz waves. *Geophysical Research Letters*, *43*, 5635–5643. https://doi.org/10.1002/2016GL069192

Li, W. Y., Guo, X. C., & Wang, C. (2012). Spatial distribution of Kelvin-Helmholtz instability at low-latitude boundary layer under different solar wind speed conditions. *Journal of Geophysical Research*, *117*, A08230. https://doi.org/10.1029/2012JA017780

Ma, X., Otto, A., & Delamere, P. A. (2014a). Interaction of magnetic reconnection and Kelvin-Helmholtz modes for large magnetic shear: 1. Kelvin-Helmholtz trigger. *Journal of Geophysical Research: Space Physics*, *119*, 781–797. https://doi.org/10.1002/2013JA019224

Ma, X., Otto, A., & Delamere, P. A. (2014b). Interaction of magnetic reconnection and Kelvin-Helmholtz modes for large magnetic shear: 2. Reconnection trigger. *Journal of Geophysical Research: Space Physics*, *119*, 808–820. https://doi.org/10.1002/2013JA019225

Ma, X., Stauffer, B., Delamere, P. A., & Otto, A. (2015). Asymmetric Kelvin-Helmholtz propagation at Saturn's dayside magnetopause. *Journal of Geophysical Research: Space Physics*, *120*, 1867–1875. https://doi.org/10.1002/2014JA020746

Ma, X., Otto, A., Delamere, P. A., & Zhang, H. (2016). The interaction between reconnection and Kelvin-Helmholtz in the high-latitude magnetopause. *Advances in Space Research*, *58*(2), 231–239. https://doi.org/10.1016/j.asr.2016.02.025

Ma, X., Otto, A., & Delamere, P. A. (2016). Plasma transport driven by the Rayleigh-Taylor instability. *Journal of Geophysical Research: Space Physics*, *121*, 5260–5271. https://doi.org/10.1002/2015JA022122

Masters, A., Achilleos, N., Bertucci, C., Dougherty, M., Kanani, S., Arridge, C., … Coates, A. (2009). Surface waves on Saturn's dawn flank magnetopause driven by the Kelvin-Helmholtz instability. *Planetary and Space Science*, *57*(14-15), 1769–1778. https://doi.org/10.1016/j.pss.2009.02.010

Merkin, V. G., Lyon, J. G., & Claudepierre, S. G. (2013). Kelvin-Helmholtz instability of the magnetospheric boundary in a three-dimensional global MHD simulation during northward IMF conditions. *Journal of Geophysical Research: Space Physics*, *118*, 5478–5496. https://doi.org/10.1002/jgra.50520

Miura, A. (1982). Nonlinear evolution of the magnetohydrodynamic Kelvin-Helmholtz instability. *Physical Review Letters*, *49*, 779.

Miura, A. (1984). Anomalous transport by magnetohydrodynamic Kelvin-Helmholtz instabilities in the solar wind-magnetosphere interaction. *Journal of Geophysical Research*, *89*, 801–818. https://doi.org/10.1029/JA089iA02p00801

Nakamura, T. K. M., & Fujimoto, M. (2005). Magnetic reconnection within rolled-up MHD-scale Kelvin-Helmholtz vortices: Two-fluid simulations including finite electron inertial effects. *Geophysical Research Letters*, *32*, L21102. https://doi.org/10.1029/2005GL023362

Nakamura, T. K. M., Fujimoto, M., & Otto, A. (2006). Magnetic reconnection induced by weak Kelvin-Helmholtz instability and the formation of the low-latitude boundary layer. *Geophysical Research Letters*, *33*, L14106. https://doi.org/10.1029/2006GL026318

Nakamura, T. K. M., Fujimoto, M., & Otto, A. (2008). Structure of an MHD-scale Kelvin-Helmholtz vortex: Two-dimensional two-fluid simulations including finite electron inertial effects. *Journal of Geophysical Research*, *113*, A09204. https://doi.org/10.1029/2007JA012803

Nakamura, T. K. M., Daughton, W., Karimabadi, H., & Eriksson, S. (2013). Three-dimensional dynamics of vortex-induced reconnection and comparison with THEMIS observations. *Journal of Geophysical Research: Space Physics*, *118*, 5742–5757. https://doi.org/10.1002/jgra.50547

Nykyri, K., & Otto, A. (2001). Plasma transport at the magnetospheric boundary due to reconnection in Kelvin-Helmholtz vortices. *Geophysical Research Letters*, *28*, 3565–3568. https://doi.org/10.1029/2001GL013239

Nykyri, K., & Otto, A. (2004). Influence of the Hall term on KH instability and reconnection inside KH vortices. *Annales de Geophysique*, *22*, 935–949. https://doi.org/10.5194/angeo-22-935-2004

Nykyri, K., Otto, A., Lavraud, B., Mouikis, C., Kistler, L. M., Balogh, A., & Rème, H. (2006). Cluster observations of reconnection due to the Kelvin-Helmholtz instability at the dawnside magnetospheric flank. *Annales de Geophysique*, *24*, 2619–2643. https://doi.org/10.5194/angeo-24-2619-2006

Otto, A. (1990). 3D resistive MHD computations of magnetospheric physics. *Computer Physics Communications*, *59*, 185–195. https://doi.org/10.1016/0010-4655(90)90168-Z

Otto, A. (2008). Three-dimensional simulation of Kelvin-Helmholtz modes at the magnetospheric boundary. *Eos, Transactions American Geophysical Union*, *89*(53), Fall Meet. Suppl. Abstract SM53A-02a.

Otto, A., & Fairfield, D. H. (2000). Kelvin-Helmholtz instability at the magnetotail boundary: MHD simulation and comparison with Geotail observations. *Journal of Geophysical Research*, *105*, 21,175–21,190. https://doi.org/10.1029/1999JA000312

Otto, A., Büchner, J., Nikutowski, B., & Astron. Astrophys. (2007). Force-free magnetic field extrapolation for MHD boundary conditions in simulations of the solar atmosphere, *468*, 313–321. https://doi.org/10.1051/0004-6361:20054495

Potter, D. (1973). *Computational Physics*. London, New York: John Wiley.

Schindler, K., Hesse, M., & Birn, J. (1988). General magnetic reconnection, parallel electric fields, and helicity. *Journal of Geophysical Research*, *93*(A6), 5547–5557. https://doi.org/10.1029/JA093iA06p05547

Sonnerup, B. U. O. (1980). Theory of the low-latitude boundary layer. *Journal of Geophysical Research*, *85*, 2017–2026. https://doi.org/10.1029/JA085iA05p02017

Stawarz, J. E., Eriksson, S., Wilder, F. D., Ergun, R. E., Schwartz, S. J., Pouquet, A., … Sturner, A. P. (2016). Observations of turbulence in a Kelvin-Helmholtz event on 8 September 2015 by the Magnetospheric Multiscale mission. *Journal of Geophysical Research: Space Physics*, *121*, 11,021–11,034. https://doi.org/10.1002/2016JA023458

Vernisse, Y., Lavraud, B., Eriksson, S., Gershman, D. J., Dorelli, J., Pollock, C., … Yokota, S. (2016). Signatures of complex magnetic topologies from multiple reconnection sites induced by Kelvin-Helmholtz instability. *Journal of Geophysical Research: Space Physics*, *121*, 9926–9939. https://doi.org/10.1002/2016JA023051

Walsh, B. M., Thomas, E. G., Hwang, K.-J., Baker, J. B. H., Ruohoniemi, J. M., & Bonnell, J. W. (2015). Dense plasma and Kelvin-Helmholtz waves at Earth's dayside magnetopause. *Journal of Geophysical Research: Space Physics*, *120*, 5560–5573. https://doi.org/10.1002/2015JA021014

Yan, G. Q., Mozer, F. S., Shen, C., Chen, T., Parks, G. K., Cai, C. L., & McFadden, J. P. (2014). Kelvin-Helmholtz vortices observed by THEMIS at the duskside of the magnetopause under southward interplanetary magnetic field. *Geophysical Research Letters*, *41*, 4427–4434. https://doi.org/10.1002/2014GL060589